Isotopic fission-fragment distributions of ^{238}U, ^{239}Np, ^{240}Pu, ^{244}Cm, and ^{250}Cf produced through inelastic scattering, transfer, and fusion reactions in inverse kinematics

D. Ramos,[1,*] M. Caamaño,[1] F. Farget,[2,†] C. Rodríguez-Tajes,[2] L. Audouin,[3] J. Benlliure,[1] E. Casarejos,[4] E. Clement,[2] D. Cortina,[1] O. Delaune,[2,‡] X. Derkx,[5] A. Dijon,[2] D. Doré,[6] B. Fernández-Domínguez,[1] G. de France,[2] A. Heinz,[7] B. Jacquot,[2] A. Navin,[2] C. Paradela,[1,§] M. Rejmund,[2] T. Roger,[2] M.-D. Salsac,[6] and C. Schmitt[2,‖]

[1]*Universidade de Santiago de Compostela, E-15706 Santiago de Compostela, Spain*
[2]*GANIL, CEA/DSM-CNRS/IN2P3, BP 55027, F-14076 Caen Cedex 5, France*
[3]*IPN Orsay, Université de Paris Sud-CNRS/IN2P3, F-91406 Orsay Cedex, France*
[4]*Universidade de Vigo, E-36310 Vigo, Spain*
[5]*LPC Caen, Université de Caen Basse-Normandie-ENSICAEN-CNRS/IN2P3, F-14050 Caen Cedex, France*
[6]*CEA Saclay, DMS/IRFU/SPhN, 91191 Gif-sur-Yvette Cedex, France*
[7]*Chalmers University of Technology, SE-41296 Göteborg, Sweden*

(Received 15 February 2018; published 21 May 2018)

Transfer- and fusion-induced fission in inverse kinematics has proved to be a powerful tool to investigate nuclear fission, widening information on the fission fragments and access to unstable fissioning systems with respect to other experimental approaches. An experimental campaign is being carried out at GANIL with this technique since 2008. In these experiments, a beam of ^{238}U, accelerated to 6.1 MeV/u, impinges on a ^{12}C target. Fissioning systems from U to Cf are populated through inelastic scattering, transfer, and fusion reactions, with excitation energies that range from a few MeV up to 46 MeV. The use of inverse kinematics, the SPIDER telescope, and the VAMOS spectrometer allow the characterization of the fissioning system in terms of mass, nuclear charge, and excitation energy, and the isotopic identification of the full fragment distribution. This work reports on new data from the second experiment of the campaign on fission-fragment yields of the heavy actinides ^{238}U, ^{239}Np, ^{240}Pu, ^{244}Cm, and ^{250}Cf, which are of interest from both fundamental and application points of view.

DOI: 10.1103/PhysRevC.97.054612

I. INTRODUCTION

The modeling of the fission process is a very important step in the evaluation of data, because many of the nuclei of interest, in terms of application and fundamental physics, are barely accessible in experiments so far. These models, based on present measurements, must prove their reliability by comparing their predictions with new observations. In this sense, new experimental approaches that provide new observables and access to more exotic systems are desirable, in particular at low excitation energy where both the macroscopic and the microscopic aspects of the nuclear matter compete and can be observed: the deformation of the fissioning system along the path towards the scission point corresponds to a large-scale amplitude collective motion involving all nucleons of the fissioning nucleus, while the produced fragment distributions are strongly affected by shell effects close to the scission point.

Fission-fragment distributions are crucial observables for the modeling of the fission process. Nevertheless, the access to such observables was, until recently, limited to mass distributions, where the contribution of both proton and neutron numbers are mixed. Later on, the use of inverse kinematics demonstrated that systematic measurements of the nuclear charge distributions were also possible [1].

These two separated observables, mass and nuclear charge, can be used to study the role of neutrons and protons in the fission process, if measured together as isotopic fragment yields. Complete isotopic fragment distributions and their correlations with other observables are a novel and stringent test for modern fission models. So far, data on isotopic fission-fragment yields are scarce and mainly limited to light fragments due to the low kinetic energy of the fission fragments in experiments performed in direct kinematics, such as thermal neutron-induced fission [2–4]. There exist some isotopic measurements of heavy fragments by means of prompt and β-delayed γ spectroscopy, as well as radiochemical techniques, but they are limited in accuracy and in range [5–8].

A new experimental approach, which exploits the inverse kinematics technique to access the nuclear charge information and the use of a magnetic spectrometer for high-resolution measurements of the fragment mass, is currently being used in a fission campaign initiated in GANIL in 2008 using the VAMOS spectrometer [9]. In this approach, in-flight fission of heavy actinides, induced by inelastic scattering, transfer,

*Present address: IPN Orsay, Université de Paris Sud-CNRS/IN2P3, F-91406 Orsay Cedex, France; diego.ramos@usc.es
†Present address: LPC Caen, Université de Caen Basse-Normandie-ENSICAEN-CNRS/IN2P3, F-14050 Caen Cedex, France.
‡Present address: CEA/DAM/DIF, F-91297 Arpajon, France.
§Present address: EC-JRC, Institute for Reference Materials and Measurements, Retieseweg 1111, B-2440 Geel, Belgium.
‖Present address: IPHC Strasbourg, Université de Strasbourg-CNRS/IN2P3, F-67037 Strasbourg Cedex 2, France.

and fusion reactions, is used. The detection of the target-like recoil permits the reconstruction of the binary reactions in order to determine the mass, charge, and excitation energy of the fissioning system [10]. The excitation energy is assumed to be stored in the heavy fissioning system because of its higher level density compared with the light-partner recoil in the range of few tens of MeV. This assumption is validated by measuring the γ decay of the light-partner recoil [10]. The low-energy regime allows investigation of more fundamental characteristics of the fission process, such as the scission point configuration in terms of deformation and the neutron content of the nascent fragments [11].

Inverse kinematics with relativistic beams was also used recently in the SOFIA experiment at GSI, where fission was induced in flight via Coulomb excitation and spallation reactions. In this case, the high velocity of the fissioning system allows the simultaneous isotopic identification of both fragments but with very poor control on the fission excitation energy [12,13].

This work presents the results of the second experiment of the fission campaign at GANIL with an improved experimental setup. It provides a new set of measurements for several fissioning systems—^{238}U, ^{239}Np, ^{240}Pu, ^{244}Cm, and ^{250}Cf—at various, low to moderate, excitation energies. Some of these systems are difficult to study with other techniques at these excitation energies. In addition, they provide nuclear data of importance for applications, such as the development of next-generation nuclear reactors or the recycling of radioactive waste [14]. These data are also of interest for the study of exotic nuclear isotopes: since fission is a very efficient mechanism for the production of neutron-rich radioactive systems either for direct studies [15,16] or for further in-beam reactions [17,18].

The experimental method and the results obtained in this work are presented in the following. The new and improved experimental setup is discussed in Sec. II. The identification of the fissioning system, together with the reconstruction of its initial excitation energy, is described in Sec III A, followed by the identification of the fission fragments, presented in Sec. III B. The determination of the fission yields, taking into account the spectrometer acceptance and efficiency corrections, is explained in Sec. III C. In Sec. IV A, the isotopic fission yields of the systems investigated in this work are reported and compared with previous measurements. Elemental and mass yields are addressed in Secs. IV B and IV C, respectively. Finally, the conclusions of this work are summarized in Sec. V.

II. EXPERIMENTAL SETUP

In this experiment, a stable $^{238}U^{+31}$ beam was produced and accelerated at GANIL up to 6.14 MeV/u with a final beam intensity of 10^9 pps. It impinged on a ^{12}C target with a thickness of 100 μg/cm^2. The average energy of the ^{238}U projectiles when the reaction takes place in the center of the target was 6.11 MeV/u, 8.2% above the s-wave Coulomb barrier between ^{238}U and ^{12}C. In such a configuration, fusion and transfer reactions, as well as elastic and inelastic scattering, take place while other channels, such as breakup reactions, are strongly suppressed. Once the reaction occurs, the beam-like

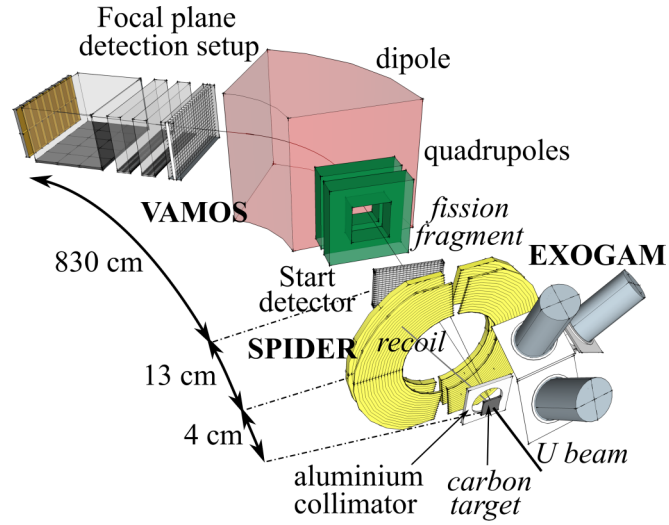

FIG. 1. Experimental setup scheme. The thick black line on the right side represents the beam impinging on the target. A transfer reaction is shown followed by a fission decay; the three thin lines represent the target-like recoil and the two fission fragments. The recoil is stopped in the SPIDER detector while one of the fission fragments triggers the start detector and passes the VAMOS spectrometer before being measured with the focal-plane detection setup. The EXOGAM detector, for γ-rays measurements, is also shown surrounding the target (for clarity, only three EXOGAM clovers are indicated).

product may decay in flight by fission whenever the excitation energy allows it.

According to the inverse kinematics, both fission fragments were emitted to forward angles in the laboratory reference frame within a cone of 28° around the beam axis, with energies ranging from a few hundred of MeV up to one GeV, whereas the target-like recoil from transfer or inelastic reactions was more likely emitted at higher angles with energies from tens of MeV up to a few hundred MeV.

The experimental setup is described in Fig. 1. Two separate stages are distinguished: the first one, which comprises an annular silicon telescope (SPIDER), was dedicated to the identification of the fissioning system; the second one, which comprises the variable mode spectrometer VAMOS, was dedicated to the measurement of the characteristics of the fission fragments. The SPIDER telescope is composed of two double-sided annular Si detectors, 70 and 1042 μm thick, respectively, which cover polar angles between 30° and 47°. The target-like recoil is detected in the SPIDER telescope where its isotopic identification is achieved by measuring both ΔE and E. The central hole of the detector ensured the noninterception of beam-like nuclei and fission fragments. Each detector is segmented into 16 rings of 1.5 mm pitch and 16 sectors, each covering a range of 22.5° in the azimuthal angle. This segmentation provides a measurement of both polar and azimuthal angles, permitting the reconstruction of the binary reaction and thus an event-by-event measurement of the excitation energy with an uncertainty of ~1 MeV [10]. A fusion reaction, ten times more frequent than any transfer channel [19], is assumed for every fission event that is registered without any target-like recoil detected in the telescope.

When the compound nucleus, produced either by transfer or fusion, decays by fission, one of the fragments may trigger the start detector, a multiwire parallel plate avalanche counter, placed at the entrance of the VAMOS spectrometer, that provides a time reference for the time-of-flight measurement. When the acceptance allows it, the fragment is deflected in the VAMOS spectrometer and fully identified in terms of mass (A), atomic number (Z), and ionic charge state (q) at the focal plane setup, placed about 7600 mm from the target, following the central trajectory of the spectrometer. The focal plane setup comprises an ensemble of detectors with an active area of 1000×150 mm^2 that includes the following: a multiwire parallel plate avalanche counter, filled with isobutane gas (iC_4H_{10}) at 7 mbar, that provided the fragment time-of-flight; two drift chambers, filled with the same gas and pressure and separated by 119.5 mm, that detected the transversal positions in each chamber and both polar and azimuthal angles (θ, ϕ); a segmented ionization chamber, filled with isobutane gas at 40 mbar, that measured the energy loss of the fragment; and an array of 20×2 silicon detectors that measured the remaining energy of the fragments stopped in this array (see Refs. [20,21] for further details).

Finally, six clovers of the EXOGAM detector [22] were placed surrounding the target for detection of prompt γ rays. This measurement provides a verification of the fragment identification done with VAMOS [23], as well as the study of the excited states populated in the target-like nuclei [10].

III. ANALYSIS

The analysis of the data obtained in this experiment is split in three different stages: in Sec. III A, the isotopic identification of the fissioning system and the determination of its kinematics and excitation energy by characterizing the binary reaction reconstructed in SPIDER are described; in Sec. III B, the isotopic identification of the fission fragment detected in the focal-plane setup of the VAMOS spectrometer is presented; and finally, in Sec. III C, the detection efficiency and acceptance corrections required to obtain the isotopic fission-fragment yields of each fissioning system are discussed.

A. Fissioning-system identification

The beam-like scattered nuclei produced by transfer reactions are identified by detecting the target-like recoil in the SPIDER detector. This detector provides their isotopic identification by measuring the energy loss in the first stage and the remaining energy in the last stage of the detector. The segmentation of the detector provides also a measurement of the recoil angles.

Figure 2 presents the isotopic identification of the recoil nuclei produced in coincidence with the detection of one fission fragment in the VAMOS setup. The energy loss, corrected for the polar angle in order to account for the effective thickness crossed by the recoil, is displayed as a function of the total kinetic energy. Each isotopic line corresponds to one transfer channel that straightforwardly determines the mass and the charge of the heavy fissioning nucleus. The most abundant and accessible reaction channels are displayed in Table I.

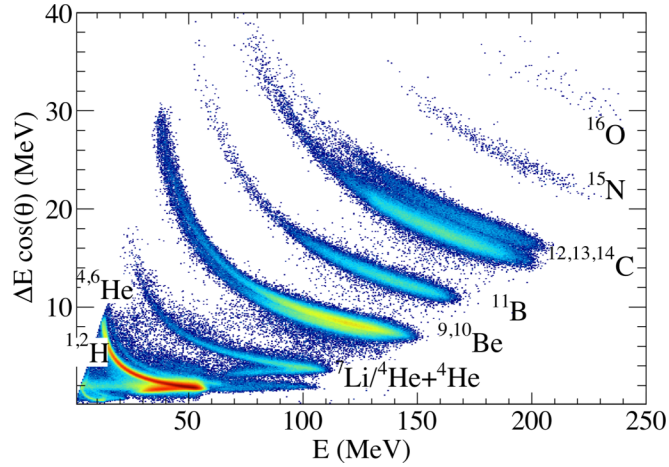

FIG. 2. Isotopic identification of the target-like recoil nuclei in the SPIDER detector in coincidence with the detection of one fission fragment in the VAMOS setup.

The measurement of the kinetic energy and the polar angle of each recoil, together with its identification, allows the reconstruction of the binary reaction, event by event, and the determination of the excitation energy (E_x), the velocity ($V_{\rm fiss}$), and the polar angle ($\theta_{\rm fiss}$) of the fissioning system, based on energy-momentum conservation [10].

Figure 3 displays the kinematics of the transfer-fission channels in terms of the velocity and the polar angle of the fissioning system with respect to the beam axis. The figure also displays the kinematics of the elastic channel, which is measured in random coincidences between an elastically scattered ^{12}C detected in SPIDER and a fragment from fusion-fission detected in VAMOS.

Table I shows the average value and the standard deviation of E_x for the different fissioning systems investigated in this work. They are obtained from the full excitation energy distributions measured in this experiment, described in Ref. [10]. The excitation of the target-like recoils was also investigated by means of γ-decay spectroscopy [10], where the probability for a fission event from an excited heavy scattered nucleus and a cold light recoil was observed to be $P > 0.86$ in the case of ^{238}U, ^{239}Np, and ^{240}Pu; in the case of ^{244}Cm, the neutron separation energy of the partner, $S_n(^6\text{He}) = 1.7$ MeV, is lower than the first excited state, which prevents the detection of excited recoils. This observation indicates that the E_x released

TABLE I. Sample of fissioning systems produced in $^{238}\text{U} + ^{12}\text{C}$ reactions and studied in this work. The average value and measured standard deviation of the excitation energy distribution are indicated for each channel.

Transfer reaction	$\langle E_x \rangle$ (MeV)	SD_{E_x} (MeV)
$^{12}\text{C}(^{238}\text{U},^{238}\text{U})^{12}\text{C}$	7.4	3.0
$^{12}\text{C}(^{238}\text{U},^{239}\text{Np})^{11}\text{B}$	7.5	2.8
$^{12}\text{C}(^{238}\text{U},^{240}\text{Pu})^{10}\text{Be}$	10.7	3.0
$^{12}\text{C}(^{238}\text{U},^{244}\text{Cm})^{6}\text{He}$	23.0	3.7
$^{12}\text{C}(^{238}\text{U},^{250}\text{Cf})$	46.0	0

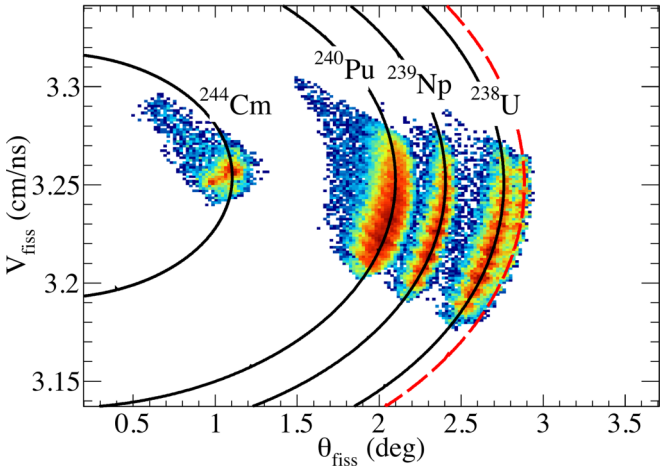

FIG. 3. Kinematics of transfer-fission channels detected in SPIDER. The solid black lines represent the theoretical kinematical lines corresponding to the most populated excitation energy, while the dashed red line corresponds to the kinematics of the random coincidence between an elastic scattered recoil with a fusion-fission event.

in the primary reaction is mainly stored in the fissioning system, as we shall assume in this work, which validates these surrogate reactions in terms of energy, compared with neutron-induced fission.

B. Fission-fragment identification

As discussed in Sec. III C 1, the VAMOS spectrometer is able to accept one fragment per fission, which is deflected according to its magnetic rigidity ($B\rho$) and its initial polar and azimuthal angles (θ,ϕ), before is detected at the focal plane. The ion optics of the spectrometer defines a relation between its initial properties ($B\rho$,θ,ϕ) and the final transversal positions and angles of the fragment at the focal plane. A reconstruction method is applied, based on the positions and angles at the focal plane, in order to obtain the initial observables ($B\rho$,θ,ϕ), as well as the path length of the fragment [24].

$B\rho$ relates the mass (A) over the ionic charge state (q) to the velocity ($\beta\gamma$) of the fragment,

$$A/q = \frac{B\rho}{3.105\ [\mathrm{T\,m}] \times \beta\gamma}, \tag{1}$$

where $\beta\gamma$ is calculated from the time of flight and the path length of the fragment.

Independently, the mass of the fragment is determined from the measurement of the total kinetic energy,

$$A^m = \frac{E}{u \times (\gamma - 1)}, \tag{2}$$

where u is the atomic mass unit and $E = \Delta E + E_{\mathrm{res}}$ is the total kinetic energy, with ΔE the energy loss in the ionization chamber, corrected for the energy loss released in the different windows and passive layers of matter, and E_{res} the remaining energy released in the silicon array.

The combination of both observables, A and A/q, allows the extraction the charge state value and provides a measurement of the mass with higher resolution than the one obtained directly from the energy and velocity.

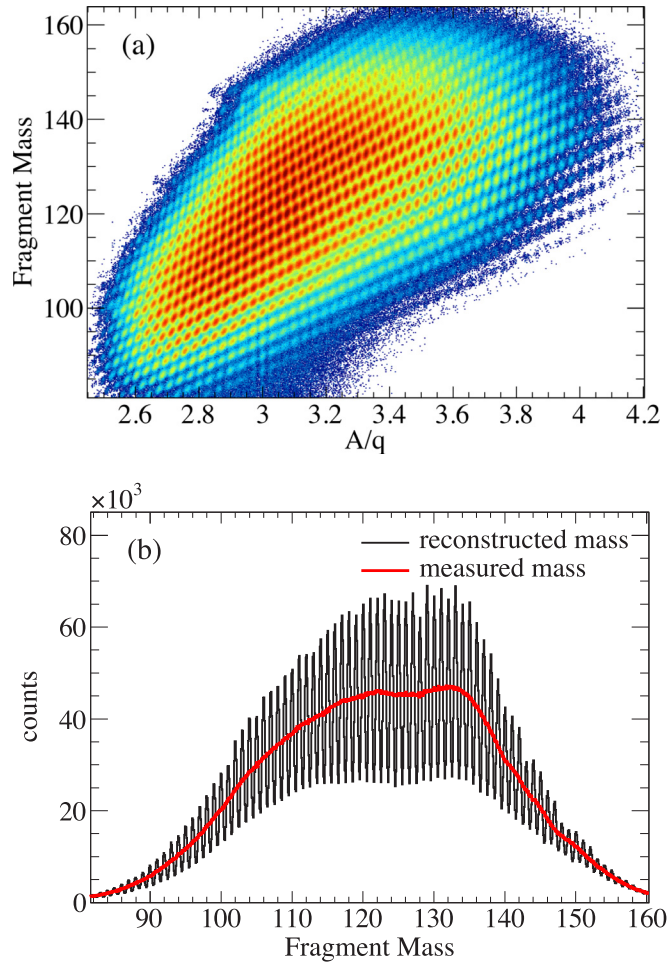

FIG. 4. (a) Identification of mass and charge state of fission fragments from fusion-fission reactions. (b) Mass distributions of fission fragments from fusion-fission reactions. The masses reconstructed from the magnetic rigidity (in black) are compared with the direct measurement (in red).

Figure 4(a) shows the mass and charge state identification of fragments from fusion-fission reactions. Each diagonal line corresponds to a specific charge state q, while the different spots refer to different masses for a given q.

The charge state distribution, calculated as

$$q = A^m/(A/q), \tag{3}$$

presents a resolution of $\mathrm{FWHM}_q/q = 1.4\%$ for the central values.

The reconstructed mass (A^{rec}) is obtained with the integer value of each charge state,

$$A^{\mathrm{rec}} = q^{\mathrm{int}} \times (A/q), \tag{4}$$

where $q^{\mathrm{int}} = \lfloor q + 0.5 \rfloor$ is the closest integer value to q.

Figure 4(b) presents the mass distribution of fragments from fusion-fission. The red line indicates the masses obtained from the direct measurement (A^m), where no mass separation is possible. The black distribution represents the masses obtained from the reconstruction method (A^{rec}). The resolution of A^{rec}

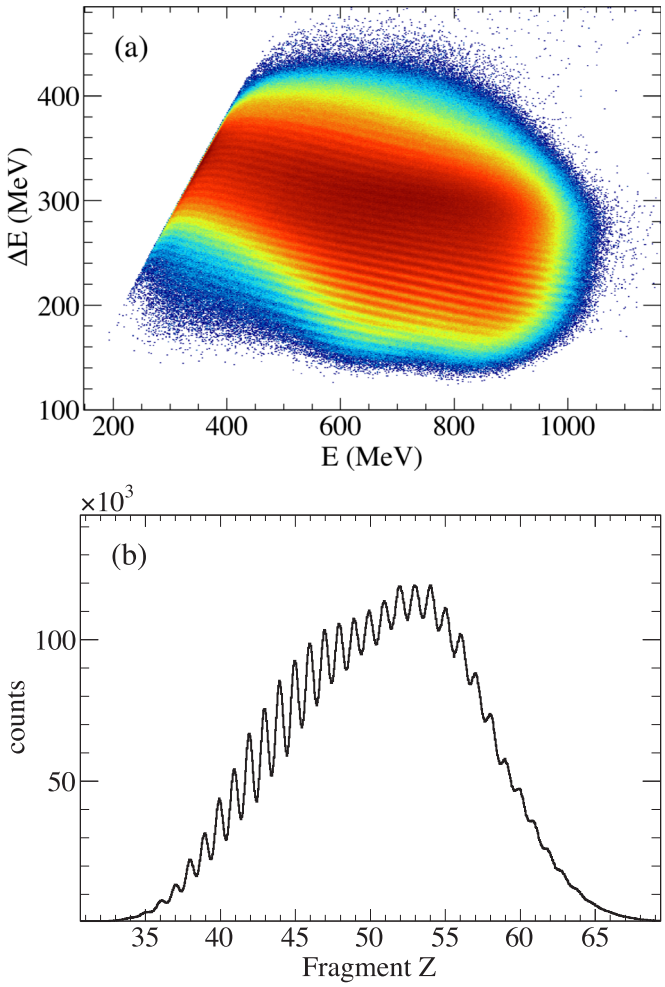

FIG. 5. (a) Relation between the energy loss and the total kinetic energy of fission fragments from fusion-fission reactions. Each curve represents one nuclear charge. (b) Nuclear charge distribution of fission fragments from fusion-fission reactions.

is determined by the time-of-flight resolution that evolves from $\mathrm{FWHM}_A/A = 0.8\%$ or the faster lighter fragment to $\mathrm{FWHM}_A/A = 0.5\%$ for the slower heavier fragments.

The identification of the atomic number (Z) of fission fragments is based on the relation between the energy loss of the fragment in the ionization chamber (ΔE) and the total kinetic energy (E). Figure 5(a) represents ΔE as a function of E for fission fragments from fusion-fission reactions. Each element defines a curve that ranges from the *Bragg peak*, at lower energies, up to hundreds of MeV. The heavier elements, at higher ΔE, are seen to be less separated from each other due to the lower intrinsic resolution for such slow nuclides.

The Z distribution is obtained from a parametrization of the full range of the ΔE-E distribution [25]. Figure 5(b) presents the Z distribution of fragments from fusion-fission reactions, where the final Z resolution results in a rather constant value, $\mathrm{FWHM}_Z/Z = 1.8\%$.

The (Z,A) identification of the fission fragments is confirmed by measuring the energy of γ rays emitted in the decay of known excited estates of even-even nuclei [23,25].

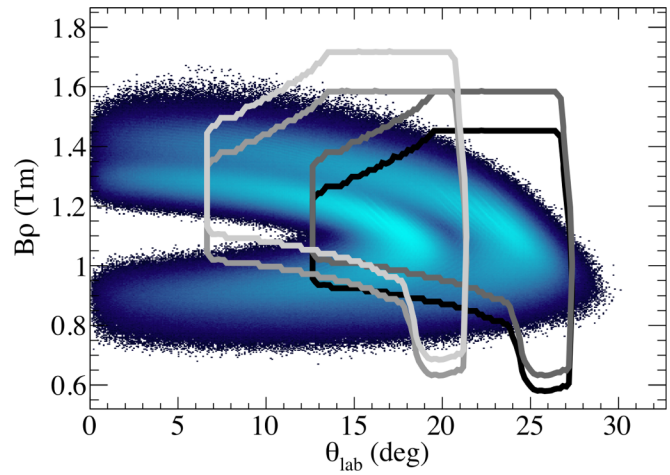

FIG. 6. Acceptance of VAMOS in terms of magnetic rigidity and polar angle. The four settings used in the experiment are displayed on top of a simulation of the fragment distribution produced from transfer-induced fission.

C. Reconstruction of fission-fragment yields

The isotopic fission-fragment identification presented above permits to determine the isotopic fission-fragment yields, $Y(Z,A)$, defined as the normalized production of one particular (Z,A) fragment per fission. They are calculated from the number of events of each isotope measured during the experiment, corrected by the geometric (ε_g^{ff}) and intrinsic (ε_i^{ff}) efficiencies for fission fragment detection.

ε_g^{ff} is determined by the angular and the magnetic rigidity acceptance of VAMOS while ε_i^{ff} is determined by the response of the detectors.

1. VAMOS acceptance

In this experimental configuration, the magnetic rigidity of fission fragments is a broad distribution due to the combination of wide distributions of momentum and ionic charge, as described in Ref. [9]. In addition, the angular distribution of fragments in the laboratory frame covers a polar angle range from 0° to 28°. Therefore, the detection is limited to one single fragment, and the large acceptance of VAMOS— ±30 % in momentum and ±5.7° in polar angle [21]—is not sufficient to cover the full fragment distribution. Instead, different settings in magnetic field and central angle were used during the experiment in order to enlarge the variety and range of the measured fragments. Figure 6 presents the acceptance of VAMOS in terms of magnetic rigidity and polar angle for the four settings used in this experiment superimposed on a Monte Carlo simulation of the expected fission-fragment distribution. Two settings with central magnetic rigidities $B\rho_0 = 1.1$ and 1.2 Tm were used with VAMOS rotated at 20° with respect to the beam axis. These settings have a large acceptance for light fragments. Two other settings with $B\rho_0 = 1.2$ and 1.3 Tm were used with VAMOS rotated at 14° to increase the acceptance for heavy fragments.

Normalization with respect to the beam current is computed between the different settings with the measurement of

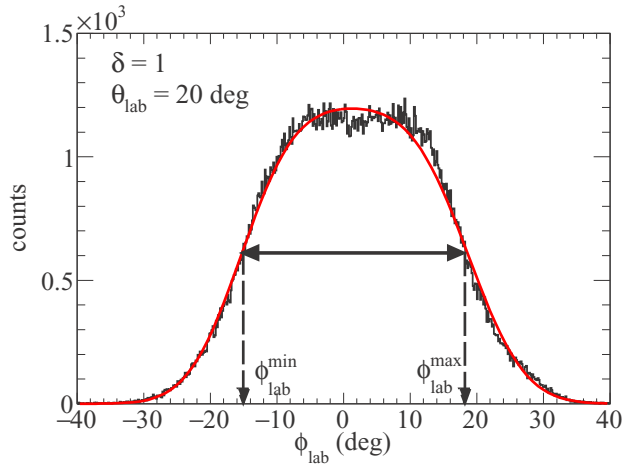

FIG. 7. $\phi_{\rm lab}$ distribution of the fragments accepted in VAMOS for $\delta \in (0.995,1.005)$ and $\theta_{\rm lab} \in (19.75,20.25)$ deg. The red line represents the function fitted to the distribution, where $\phi_{\rm lab}^{\rm min}$ and $\phi_{\rm lab}^{\rm max}$ define the limits of the distribution.

the elastic scattering in SPIDER for each VAMOS setting. The geometric and intrinsic efficiency of SPIDER, as well as the thickness of the target, are considered constant during the experiment.

Concerning the azimuthal angle, the focusing of the trajectories of the fission fragments when they pass through the spectrometer defines a magnification factor between the incoming azimuthal angle ($\phi_{\rm lab}$) and the outgoing angle in the vertical axis. This focusing varies with the polar angle ($\theta_{\rm lab}$) and the relative magnetic rigidity ($\delta = B\rho/B\rho_0$). Therefore, the limitation defined by the size of the detectors in the vertical axis at the focal plane is transformed into a limitation in $\phi_{\rm lab}$ at the entrance of VAMOS that evolves with $\theta_{\rm lab}$ and δ.

The physical $\phi_{\rm lab}$ distribution of a given $\theta_{\rm lab}$ and δ is a flat distribution that extends from -180° to 180°; however, the VAMOS acceptance reduces this range. In order to evaluate the accepted range, the measured $\phi_{\rm lab}$ distributions were fitted with a double *error function*, with the range of $\phi_{\rm lab}$ accepted by VAMOS defined as the *full width at half maximum* of the function. Figure 7 shows the distribution of $\phi_{\rm lab}$ for fission fragments with $\delta \in (0.995,1.005)$ and $\theta_{\rm lab} \in (19.75^\circ,20.25^\circ)$, and the function fitted with the distribution that defines the limits of the $\phi_{\rm lab}$ acceptance.

The ϕ acceptance (f_ϕ) is defined as the ratio between the range of $\phi_{\rm lab}$ accepted in VAMOS and the total physical $\phi_{\rm lab}$ range covered by fission fragments:

$$f_\phi(\theta_{\rm lab},\delta) = \frac{\left|\phi_{\rm lab}^{\rm max} - \phi_{\rm lab}^{\rm min}\right|}{360^\circ}. \quad (5)$$

A two-dimensional $\phi_{\rm lab}$ acceptance grid is obtained with a step width of 0.25° in $\theta_{\rm lab}$ and 0.005 in δ, where both angular settings of VAMOS are treated independently. The $\phi_{\rm lab}$ acceptance correction is applied, event by event, by means of a local multivariable interpolation method.

Concerning the $(B\rho,\theta_{\rm lab})$ phase space, the low beam energy prevents the emission of fully stripped fission fragments. Instead, each individual (Z,A) yield is spread over a distribution of charge states that evolves with the velocity of the fragments in the laboratory reference frame [26]. The production of each q is limited to a determined range of $(B\rho,\theta_{\rm lab})$ phase space that may be cut by the VAMOS acceptance [9].

This two-dimensional phase space can be translated into one single observable: the polar angle in the reference frame of the fissioning system ($\theta_{ff}^{\rm c.m.}$). In this frame, a different q populates a different range of $\cos(\theta_{ff}^{\rm c.m.})$. The regions of $\cos(\theta_{ff}^{\rm c.m.})$ where any q is cut are excluded from the calculation of isotopic yields while the remaining range determines the acceptance of VAMOS in the $(B\rho,\theta_{\rm lab})$ phase space.

The quantity $\cos(\theta_{ff}^{\rm c.m.})$ is determined from the velocity of the fissioning system ($\beta_{\rm fiss}$), and the velocity ($\beta_{ff}^{\rm lab}$) and polar angle ($\theta_{ff}^{\rm lab}$) of the fragment with respect to the fissioning system in the *laboratory* frame, where $\beta_{ff}^{\rm lab}$ is corrected for the energy loss in the target through a parametrization of the stopping range of heavy ions in matter [27], adapted to this experimental configuration by means of a LISE++ simulation [28]. The target thickness was chosen to be very thin in order to minimize this correction as much as possible.

For each q, the limits of the VAMOS acceptance in the $(B\rho,\theta_{\rm lab})$ phase space define a limited range of $\cos(\theta_{ff}^{\rm c.m.})$. The limits of $\cos(\theta_{ff}^{\rm c.m.})$ are calculated with an uncertainty lower than 2% from the limits of the acceptance, $B\rho|_{\rm limit}$ and $\theta_{\rm lab}|_{\rm limit}$, determined by the combination of the four settings of VAMOS presented in Fig. 6.

In the case of fusion-induced fission, both $\theta_{\rm fiss}$ and $\beta_{\rm fiss}$ are constant. Therefore, the limits of $\cos(\theta_{ff}^{\rm c.m.})$ are a function of A, q, and the limits of $B\rho$ and $\theta_{\rm lab}$: $\cos(\theta_{ff}^{\rm c.m.})|_{\rm limit} = f(A,q,B\rho|_{\rm limit},\theta_{\rm lab}|_{\rm limit})$. In the case of transfer-induced fission, the fissioning system is produced with a range of velocities and angles that need to be considered in the determination of the $\cos(\theta_{ff}^{\rm c.m.}))|_{\rm limit}$.

The charge states with the most restrictive values determine the upper and lower limits of $\cos(\theta_{ff}^{\rm c.m.})$ for a given mass. Figure 8 presents these limits as a function of the mass number. Solid and dashed lines indicate smooth functions that reproduce the upper and lower limits, respectively, in a restrictive

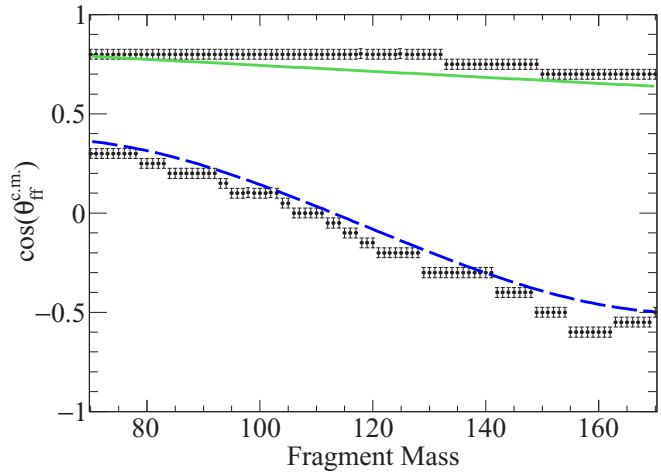

FIG. 8. Limits of $\cos(\theta_{ff}^{\rm c.m.})$ as a function of the mass number combining the four settings of VAMOS (see text for details).

way, ensuring that the full q distribution is transmitted between both limits.

The acceptance in $\theta_{ff}^{\mathrm{c.m.}}$ is thus determined by the range of $\cos(\theta_{ff}^{\mathrm{c.m.}})$ accepted by VAMOS:

$$f_{\theta_{\mathrm{c.m.}}}(A) = \frac{\left|\cos\left(\theta_{ff}^{\mathrm{c.m.}}\right)|_{\max} - \cos\left(\theta_{ff}^{\mathrm{c.m.}}\right)|_{\min}\right|}{2}(A), \quad (6)$$

where no angular anisotropy was observed.

In the case of transfer-induced fission, the velocity and angle of the fissioning system define a $\cos(\theta_{ff}^{\mathrm{c.m.}})|_{\mathrm{limit}}$ set that changes event by event. The maximum variation of $\cos(\theta_{ff}^{\mathrm{c.m.}})|_{\mathrm{limit}}$, considering the maximum and minimum velocity and angle of the fissioning system, is observed to be lower than 0.1 with respect to fusion-induced fission. Therefore, in transfer-induced fission, the range of $\cos(\theta_{ff}^{\mathrm{c.m.}})$ is assumed to be the same as in fusion-fission but conservatively reduced by 0.2.

Finally, the total geometric efficiency for the detection of fission fragments is defined as

$$\varepsilon_g^{ff} = f_\phi(\theta_{\mathrm{lab}},\delta) \times f_{\theta_{\mathrm{c.m.}}}(A). \quad (7)$$

2. Intrinsic efficiency

The intrinsic detection efficiency of fission fragments is split into three contributions corresponding to each of the involved detectors.

The intrinsic efficiency of the drift chamber depends on the energy that fission fragments deposit inside, which is lower for light fragments. This efficiency is calculated with respect to the ionization chamber and it is parametrized as a function of the energy loss in its first pad.

The intrinsic efficiency of the array of silicon detectors is affected by the malfunctioning of two detectors in the lower row during the experiment. The impact of these nonworking detectors was reflected in a lack of events in some regions of the $(B\rho,\theta_{\mathrm{lab}})$ phase space. This efficiency is corrected with respect to the phase space reconstructed from the drift chamber measurement.

Finally, the low ionization of light fragments also affects their detection in the multiwire detectors. In this case, an absolute efficiency correction is not possible since these detectors define the acquisition trigger. Instead, a relative correction is obtained by taking into account that only light fragments are affected by this reduced efficiency. Since proton evaporation before and after fission is inhibited due to the limited excitation energy, the $\cos(\theta_{ff}^{\mathrm{c.m.}})$ distribution of each light fragment (Z_1) can be normalized to the distribution of the corresponding heavy fragment ($Z_2 = Z_{\mathrm{fiss}} - Z_1$). In this case, we consider $Z_{\mathrm{fiss}} = 98$ due to the higher probability of fusion-fission reactions. The normalization was not constant in Z but a function of $(Z/v)^2$, v being the velocity of the fragment in the laboratory reference frame, which accounts for the relation between the fragment Z and its energy loss in the multiwire chamber [25].

3. Reconstruction of the charge-state distributions

Each charge-state distribution spreads among the four different settings of VAMOS used in this experiment. These settings present an overlap in some regions of $\cos(\theta_{ff}^{\mathrm{c.m.}})$ for each charge state. The number of events as a function of $\cos(\theta_{ff}^{\mathrm{c.m.}})$ in the region of overlap is chosen as the one with the largest contribution, once corrected by the efficiency:

$$N\left(Z,A,\cos\left(\theta_{ff}^{\mathrm{c.m.}}\right),q\right) = \frac{\mathrm{counts}}{\varepsilon_g^{ff} \times \varepsilon_i^{ff}}\left(Z,A,\cos\left(\theta_{ff}^{\mathrm{c.m.}}\right),q\right). \quad (8)$$

As an example, Fig. 9(a) presents the $\cos(\theta_{ff}^{\mathrm{c.m.}})$ distribution of the charge state $q = 40$ of ^{120}Sn as the overlap of the contribution of each setting.

The limits of $\cos(\theta_{ff}^{\mathrm{c.m.}})$ (presented in Fig. 8) define also the integration region where the total number of fission fragments ($N(Z,A)$) is deduced:

$$N(Z,A) = \sum_{\cos(\theta_{ff}^{\mathrm{c.m.}})|_{\min}(A)}^{\cos(\theta_{ff}^{\mathrm{c.m.}})|_{\max}(A)} N\left(Z,A,\cos\left(\theta_{ff}^{\mathrm{c.m.}}\right)\right). \quad (9)$$

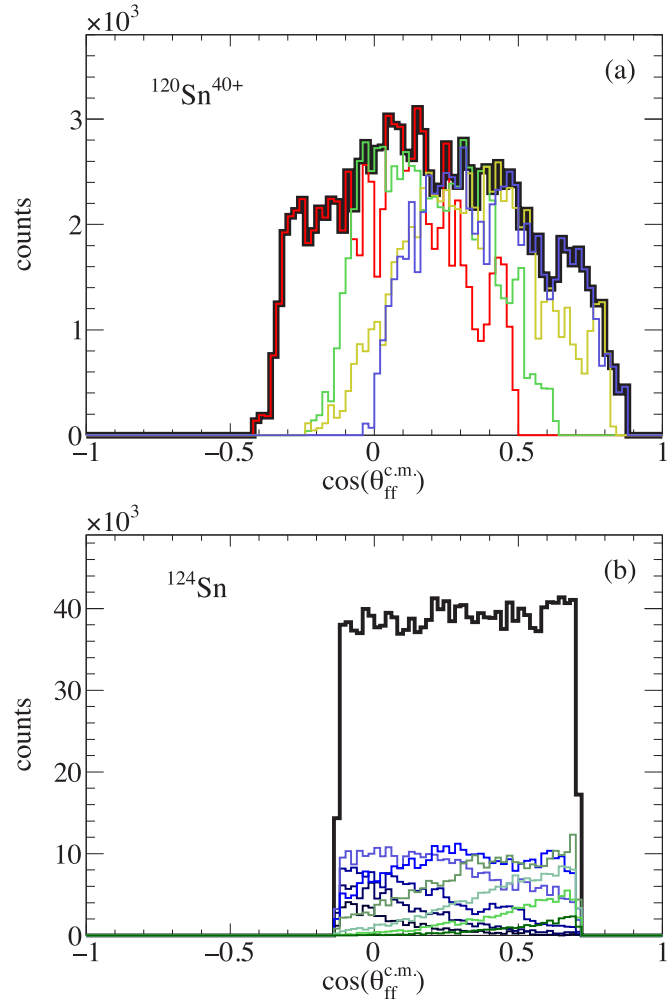

FIG. 9. (a) $\cos(\theta_{ff}^{\mathrm{c.m.}})$ distribution of the charge state $q = 40$ of ^{120}Sn. The contributions of the four settings of VAMOS are represented in color. The envelope distribution depicts the total distribution. (b) The full $\cos(\theta_{ff}^{\mathrm{c.m.}})$ distribution of ^{124}Sn within the VAMOS acceptance is presented in black, while the contribution of each q is presented in color.

The number of fission events as a function of $\cos(\theta_{ff}^{\mathrm{c.m.}})$ is obtained as the sum of the different charge state contributions:

$$N\left(Z,A,\cos\left(\theta_{ff}^{\mathrm{c.m.}}\right)\right)=\sum_{q_{\min}(A)}^{q_{\max}(A)}N\left(Z,A,\cos\left(\theta_{ff}^{\mathrm{c.m.}}\right),q\right). \quad (10)$$

In the same example, Fig. 9(b) shows, in black, the $\cos(\theta_{ff}^{\mathrm{c.m.}})$ distribution of ^{124}Sn, obtained by adding all charge states in the range of full charge state transmission. The distributions in color represent the most-populated individual charge states, from $q = 37$ to $q = 45$.

Once the total number of fission fragments is calculated, the isotopic fission-fragment yields are computed as

$$Y(Z,A)=200\times N(Z,A)\times\left(\sum_{Z,A}N(Z,A)\right)^{-1}. \quad (11)$$

IV. RESULTS

In this section, the fission yields obtained from ^{238}U + ^{12}C reactions in inverse kinematics are presented. ^{238}U, ^{239}Np, ^{240}Pu, and ^{244}Cm, populated in inelastic scattering and multinucleon transfer channels, and ^{250}Cf, from fusion reactions, are investigated.

The fusion channel dominates the total reaction cross-section, while multinucleon transfer reactions contribute approximately 10%. Under these conditions, the production rate of fission from transfer reactions with respect to fusion reactions reveals that the full efficiency of SPIDER is around 20%, leading to a contamination in the fusion channel of 8% from transfer reactions.

The inelastic scattering channel is also contaminated by the fortuitous coincidences between the detection of a recoil from an elastic scattering reaction in SPIDER and the detection of a fragment in VAMOS from a fusion-fission reaction. As demonstrated in Fig. 10, this contamination can be discriminated in terms of fragment mass in the region of $Z \approx 50$ due to the different mass population in fusion with respect to the other channels. This separation is used to evaluate these fortuitous coincidences that results in $(21.1 \pm 3.0)\%$ of the total number of ^{238}U fission events. An isotopic subtraction is performed in the full range of fragments of ^{238}U, taking into account that the contamination is proportional to the production of ^{250}Cf.

Concerning the other fissioning systems, a small contamination comes mainly from the fortuitous coincidences between

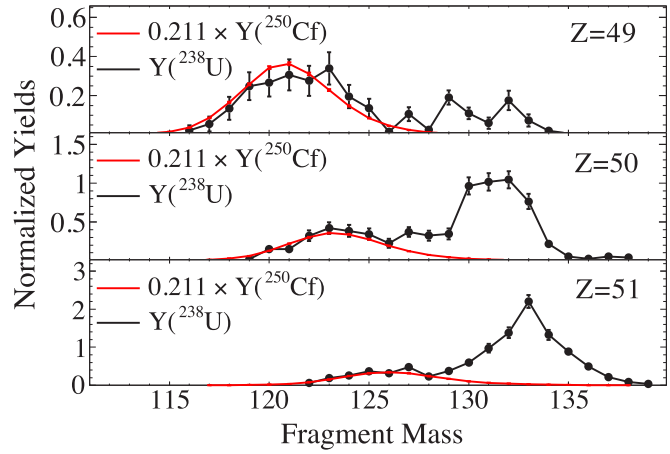

FIG. 10. The black distributions represent the isotopic yields of $Z = 49$, 50, and 51 of ^{238}U, contaminated by random coincidences between an elastic-scattered recoil detected in SPIDER and a fragment from fusion-fission detected in VAMOS. The red distributions correspond to scaled isotopic yields of ^{250}Cf, fitted with the random coincidences contamination.

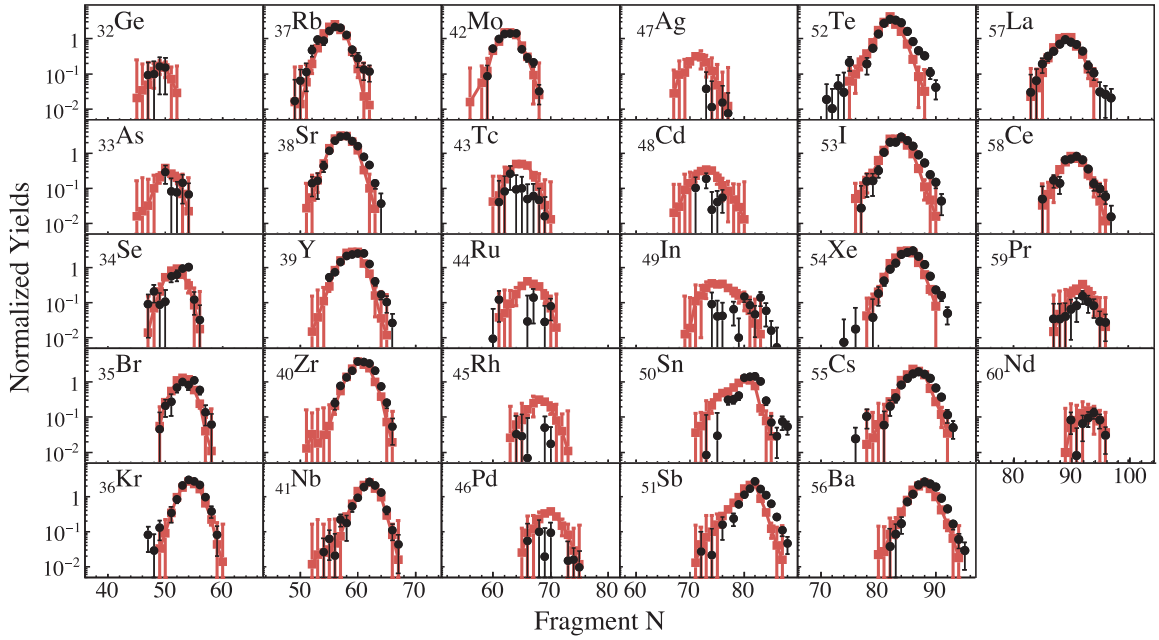

FIG. 11. Isotopic fission-fragment yields of ^{238}U ($\langle E_x \rangle = 7.4$ MeV). Present data (in black) are compared with data from Coulomb-induced fission [13] (in red).

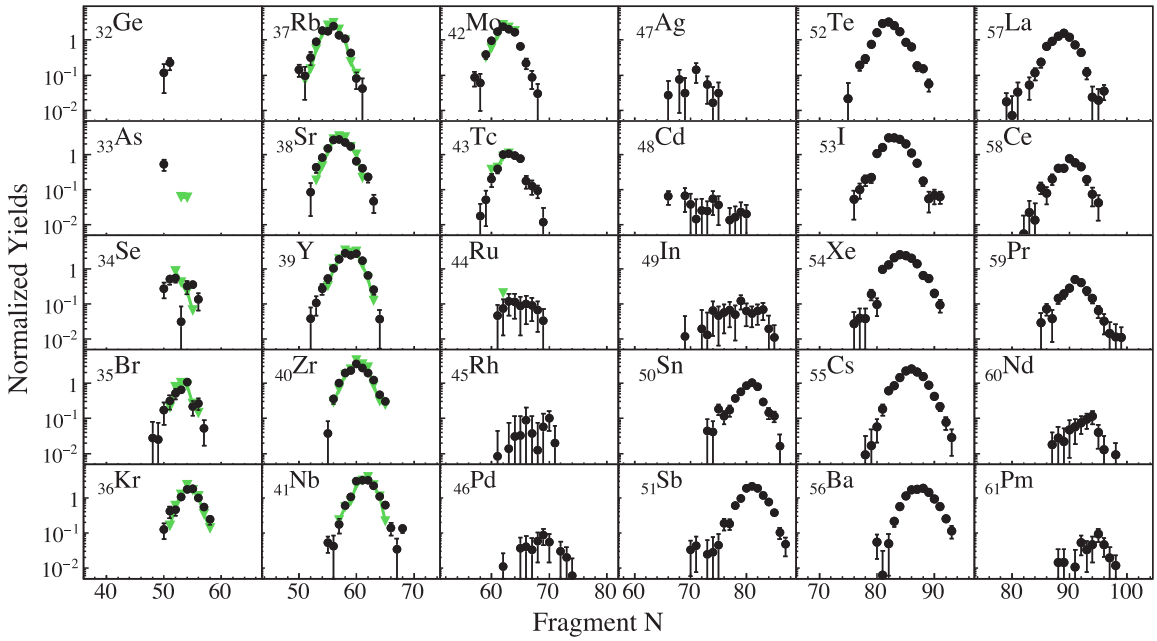

FIG. 12. Isotopic fission-fragment yields of ^{239}Np ($\langle E_x \rangle = 7.5$ MeV). Present data (in black) are compared with data from ^{237}Np($2n_{\rm th}, f$) [35] (in green).

a transfer channel with E_x lower than the fission threshold and a fission event from fusion-fission. This contamination is expected to be lower at higher E_x since the overlap in E_x between real events and fortuitous coincidences is smaller. ^{239}Np and ^{240}Pu present scarce random coincidences, $(4.0 \pm 2.1)\%$ and $(2.5 \pm 1.8)\%$ respectively, while ^{244}Cm does not exhibit a significant contamination.

The uncertainties of the final fission yields are determined as the quadratic sum of statistic and systematic sources. Systematic uncertainties range from 2% in the heavier fragments up to

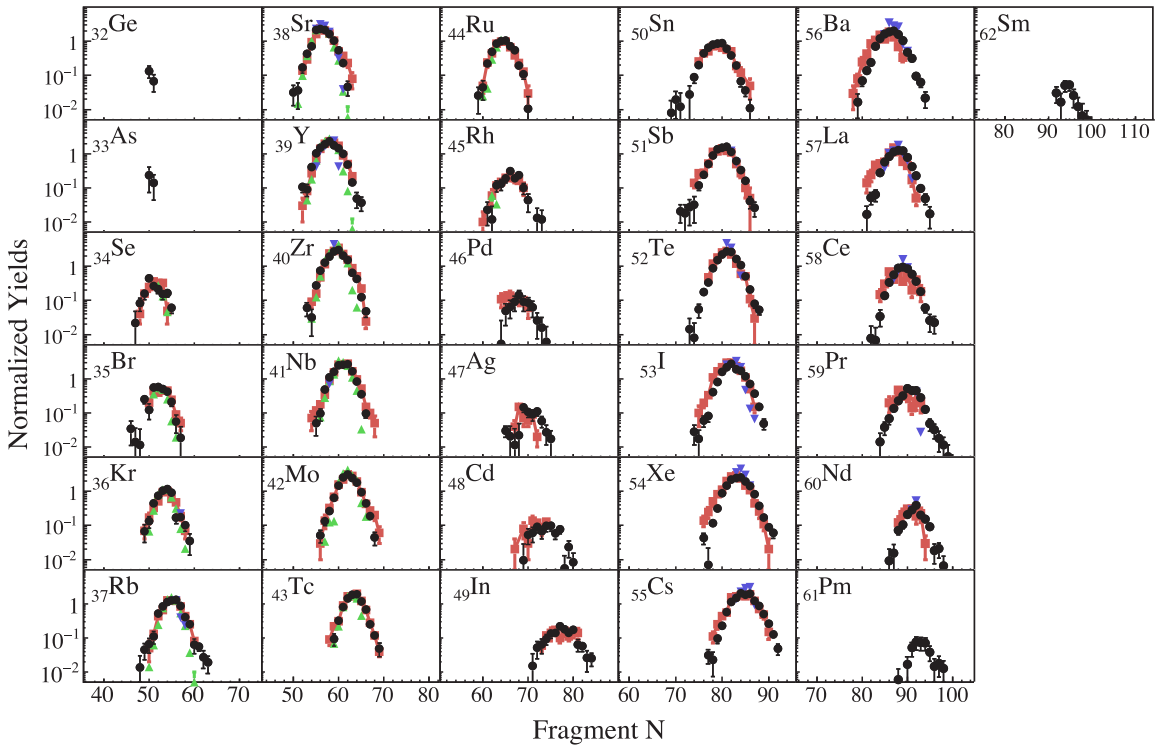

FIG. 13. Isotopic fission-fragment yields of ^{240}Pu ($\langle E_x \rangle = 10.7$ MeV). Present data (in black) are compared with data from $2p$-transfer-induced fission [9] (in red), and with ^{239}Pu($n_{\rm th}, f$) data from [29] (in green) and from [6] (in blue).

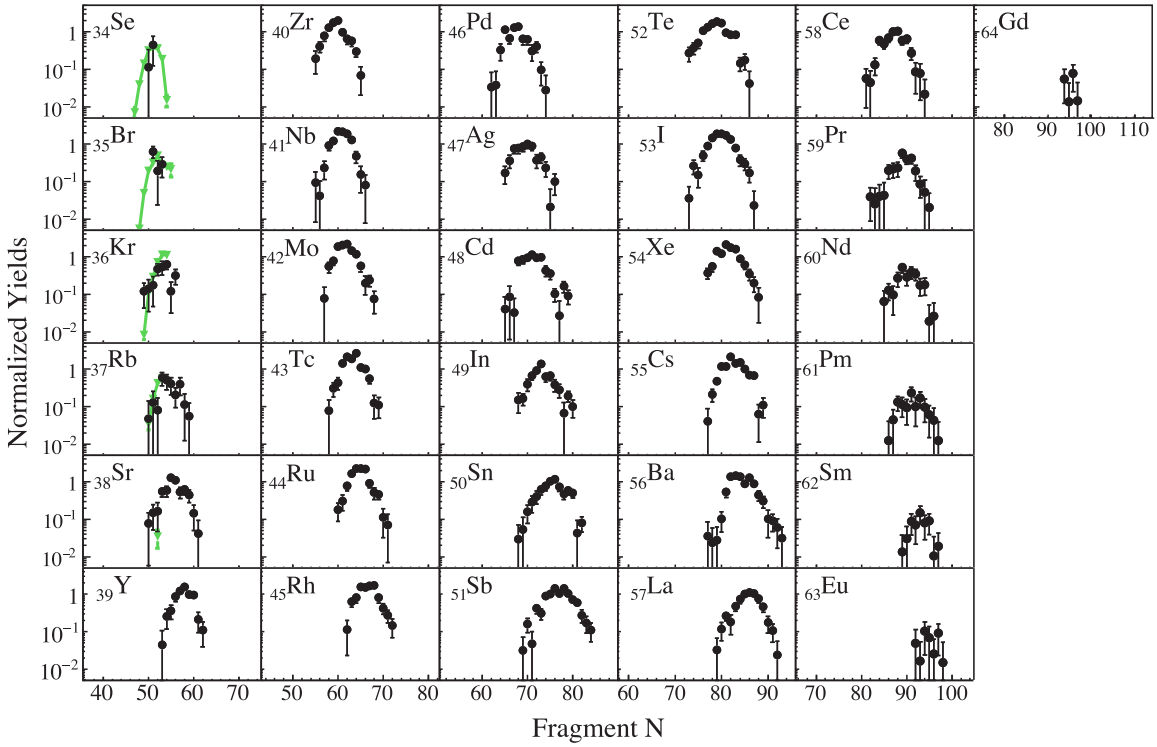

FIG. 14. Isotopic fission-fragment yields of ^{244}Cm ($\langle E_x \rangle = 23.0$ MeV). Present data (in black) are compared with the very limited data available in literature for ^{243}Cm($n_{\rm th}, f$) [30] (in green).

10% in the lighter ones. This takes into account the normalization, the determination of the ϕ acceptance, the definition of the $\cos(\theta_{ff}^{\rm c.m.})$ range, and the calculation of the intrinsic efficiency.

A. Isotopic fission-fragment yields

The full distributions of post-neutron evaporation fission yields of the five fissioning systems investigated in this work are shown in Figs. 11–15 and compared with previous measurements, whenever available. Each element is presented separately in one single plot as a function of the neutron number.

Concerning ^{238}U (Fig. 11), the present data are compared with Coulomb-induced fission from Ref. [13]. A good agreement is achieved in the region of light fragments, $Z < 43$, while around symmetry, $Z \in [43,49]$, present yields are systematically lower than in Ref. [13]. This difference can be explained by the difference in E_x [31] between the two sets of data: $\langle E_x \rangle = 7.4$ MeV in the present case, compared to an estimated $\langle E_x \rangle = 14.7$ MeV for the Coulomb-induced fission measurement. In addition, a shift in N is observed in the complementary heavy region between the two sets of data. This effect reflects the different neutron evaporation expected in this region due to the difference of $\sim$7 MeV in E_x: in a regime of constant temperature [32], the excess of E_x goes principally to the heavy fragment, which therefore evaporates more neutrons while the yields in the light region are almost unaffected, as previously observed in neutron multiplicity [33,34].

Concerning ^{239}Np (Fig. 12), the present experiment expands the available experimental data to the full distribution, whereas only light fragments were previously measured [35,36]. The previous measurement of ^{237}Np($2n_{\rm th}, f$) from Ref. [35] shows an excellent agreement with the present data, indicating that light fragments remain insensitive to the small E_x difference between the two measurements, with $\langle E_x \rangle = 7.5$ MeV and $E_x = 6.2$ MeV, respectively.

The isotopic distribution of ^{240}Pu (Fig. 13) is compared with data of $2p$-transfer-induced fission from the previous experiment of the fission campaign at VAMOS [9]. A good agreement is achieved in the full distribution range with some discrepancies in $Z > 56$, where present data overcome previous experimental limitations in measuring the heaviest fragments where only one angular setting of the spectrometer was used. Data from ^{239}Pu($n_{\rm th}, f$) from Ref. [29] (in green) and from Ref. [6] (in blue) are also included, showing a good general agreement as well.

The ^{244}Cm system is shown in Fig. 14. The population of the symmetric region in this system is more pronounced than in the above discussed systems, consistent with the higher excitation energy of $\langle E_x \rangle = 23$ MeV. Present data are compared with, to our knowledge, the only available isotopic data in literature, for ^{243}Cm($n_{\rm th}, f$) [30], which is limited to the very light fragments, $Z < 39$. The present measurement provides new data in a range of E_x where the strength of the structure effects and the liquid drop behavior are expected to be similar [37].

Finally, the isotopic yields of ^{250}Cf are presented in Fig. 15. The present data are compared with the previous measurement

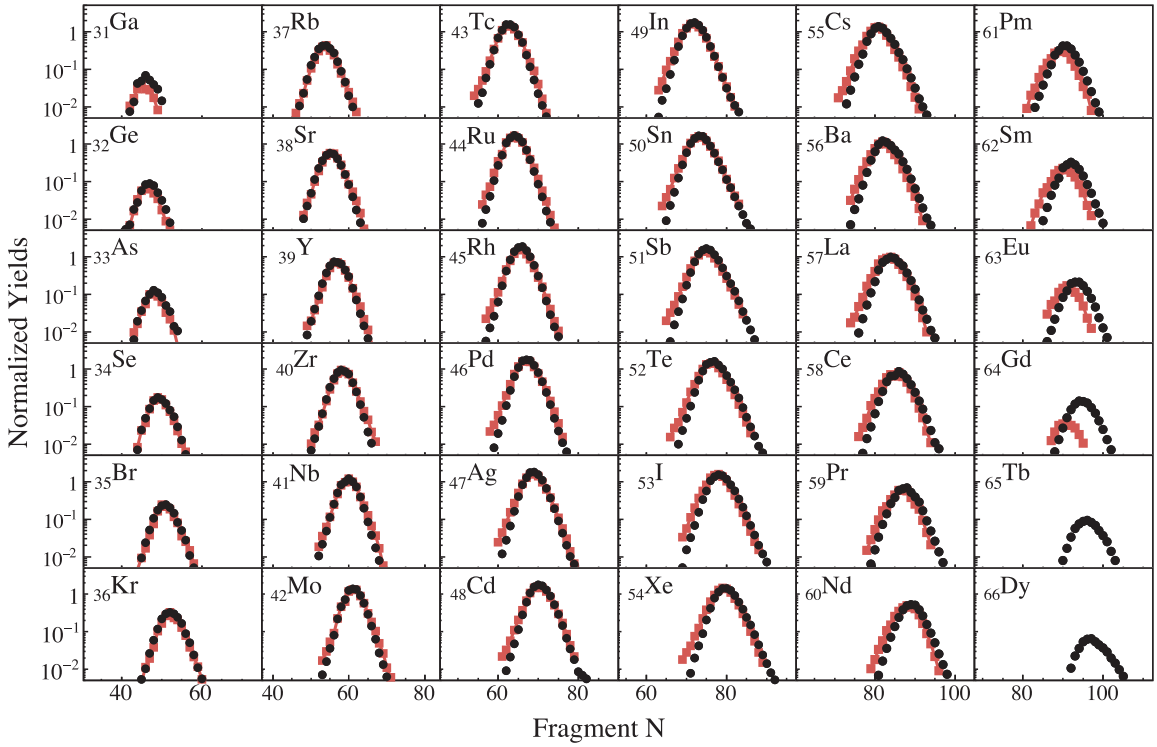

FIG. 15. Isotopic fission-fragment yields of ^{250}Cf ($E_x = 46.0$ MeV). Present data (in black) are compared with the previous measurement of fusion-induced fission [9] (in red).

performed at VAMOS [9]. A good agreement is achieved over two orders of magnitude below each maximum for the light fragments and, for the heavy fragments, the experimental limitation of the previous data (see above) is reflected in the shift of yields for $Z > 60$, when compared to the present data.

In general, the ensemble of isotopic fission yields obtained in this experiment is in good agreement with previous measurements. In addition, this experiment also represents an important step forward in the experimental access to fission yields: where isotopic yields were limited to light fragments or scarce for heavy fragments, the present work shows, for first time, the complete isotopic distribution of five different fissioning systems. In a single experiment, we can observe the evolution from a dominant asymmetric fission component at low E_x, connected to structure effects [38], to a more symmetric fission at higher E_x, indicating a stronger contribution of the macroscopic component. In addition, the new isotopic data in different ranges of E_x permit us to investigate the sharing of protons and neutrons in the fission process and the impact of E_x, which will be the topic of an upcoming publication.

B. Elemental fission-fragment yields

The elemental fission-fragment yields are obtained as the sum of the isotopic yields, defined in Eq. (11), over the mass distribution. For each element, the contamination of neighboring Z was subtracted according to the Z resolution. In addition, the elemental yields were symmetrized taking into account the statistical weight of complementary fragments.

The resulting elemental yields are depicted in Fig. 16. The systems at lower excitation energy, ^{238}U,^{239}Np, and ^{240}Pu, present a dominant asymmetric fission component with a remarkable production of $Z = 52$ in the case ^{238}U. The higher E_x of ^{244}Cm and ^{250}Cf gradually feeds the symmetric component, resulting in a quasi-Gaussian distribution for ^{250}Cf, with a plateau on the top of the distribution that indicates that the process is not yet fully determined by the liquid-drop behavior

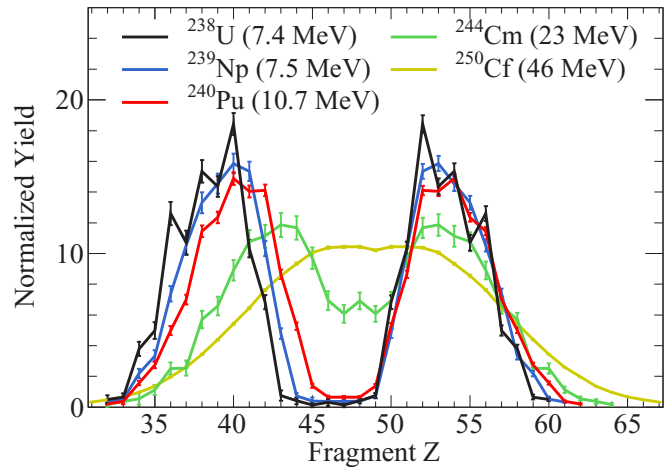

FIG. 16. Elemental fission-fragment yields. Each color represents one fissioning system, with an average excitation energy indicated in parentheses.

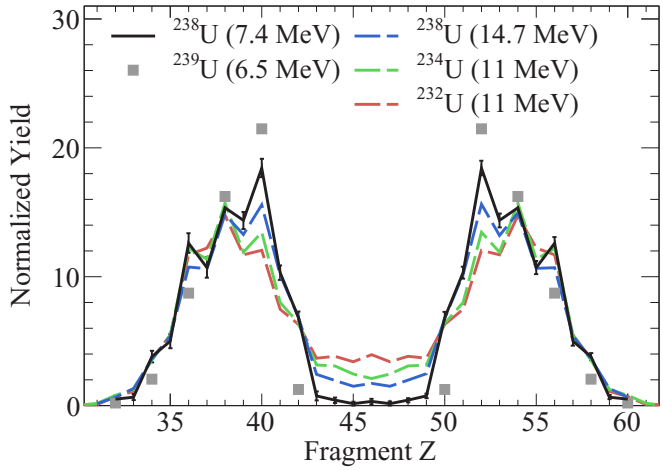

FIG. 17. Elemental fission-fragment yields of different U isotopes. Present data (in black) are compared with previous measurements at different E_x, obtained from Coulomb-induced fission [1,13] (dashed lines) and n-induced fission [41] (squares). The corresponding E_x are indicated in parentheses.

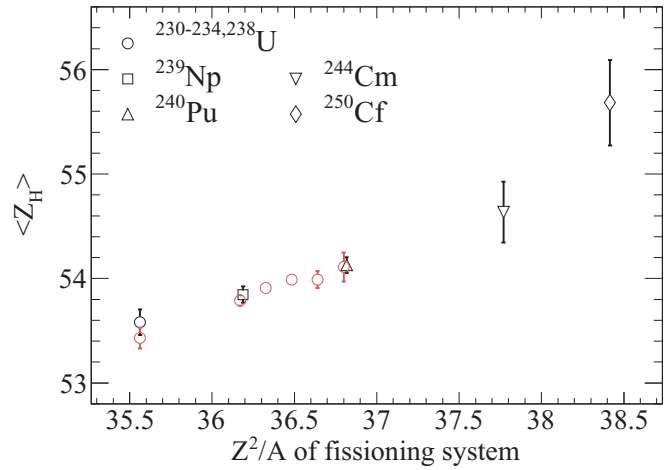

FIG. 18. Average Z value of the heavier fragment in the asymmetric fission as a function of the fissility parameter. Present data (in black) are compared with previous measurements of several U isotopes [1,13] (in red).

[39]. Instead, an effective decrease of E_x at the saddle point due to pre-saddle neutron evaporation may explain such behavior, as shown in Refs. [37,40].

Asymmetric fission at low E_x reveals a strong stabilization of the heavier fragment with an average value of $\langle Z_H \rangle = 54 \pm 0.5$, while the lighter one moves accordingly with the Z of the fissioning system. This stabilization suggests that the split at scission is mainly governed by the structure of the heavy fragment. However, the yields of ^{238}U, ^{239}Np, and ^{240}Pu present a common maximum at $Z = 40$, where the deformation at scission is very similar to the deformation of the ground state [11], which suggests an additional effect in the light group.

Interestingly, ^{238}U, ^{239}Np, and ^{240}Pu possess the same number of neutrons, $N_{\text{fiss}} = 146$. An example of the impact of the number of neutrons of the fissioning system on the elemental yields is presented in Fig. 17. Elemental yields of ^{238}U, obtained in this work, are compared with the yields of different U isotopes [1], and with the same ^{238}U isotope at higher E_x [13] from Coulomb-induced fission, and with ^{239}U [41] from neutron-induced fission. It can be observed that the reduction of the neutron content in the fissioning system has a similar impact on the elemental yields as increasing the excitation energy: symmetric fission is enhanced and the standard I (SI) fission mode, defined by Brosa *et al.* [42], centered at $Z \approx 52$ [43], is strongly suppressed. In $Z = 50$, a slight increasing trend with the neutron content of the system is observed, except in ^{239}U, where an abnormally lower yield was reported [41], which cannot be explain with this increasing trend.

The transition of the maximum yield from $Z = 54$ to $Z = 52$ in the U isotopes, if the fissioning system mass increases, as observed in Fig. 17, was recently predicted by means of the Brownian shape-motion model, with a random-walk approach on five-dimensional potential-energy surfaces [44]. In this model, the transition occurs at $A = 238$ independently of E_x of the fissioning system. A similar behavior in the evolution of the maximum of the elemental yields has been predicted in heavier actinides, such as Cf and Fm by a recent scission-point model [45] that shows a smooth variation of the potential energy surface at scission as a function of the neutron content of the fissioning system.

The average value of the heavier group ($\langle Z_H \rangle$), calculated as the average position of the asymmetric fission, is presented in Fig. 18 as a function of the fissility parameter (Z^2/A) of the fissioning system. Present data are compared with previous measurement from Coulomb-induced fission of several isotopes of uranium [1,13]. The increasing trend with the fissility parameter is similar, and the present data are in good agreement with the previous measurement for ^{238}U. This dependence reveals that the fissility is a good *ordering parameter* in which the average position of the heavy group is rather independent of the element and E_x. In the case of ^{250}Cf, the strong symmetric contribution prevents a precise measurement, and its subtraction may shift $\langle Z_H \rangle$ to a higher value.

C. Fission-fragment mass yields

Fission-fragment mass yields are obtained as the sum of the isotopic yields defined in Eq. (11) over the full Z distribution of each nuclear mass. This observable comprises both proton and neutron content, making it difficult to distinguish the role of structure effects. Nevertheless, it is useful to compare the present data with previous measurements since most of the fragment yield data in literature consist of mass distributions.

This comparison is shown in Fig. 19. In general, mass distributions present a nonsymmetric shape due to both the neutron evaporations before scission that shift the distribution to lower masses [37] and the neutron evaporation from the fragments after scission that is not constant along the fragment distribution [33,34,46].

The present ^{238}U data are compared with data from Coulomb-induced fission from Ref. [13] and from Bremsstrahlung-induced fission from Ref. [47]. The higher E_x of the Coulomb

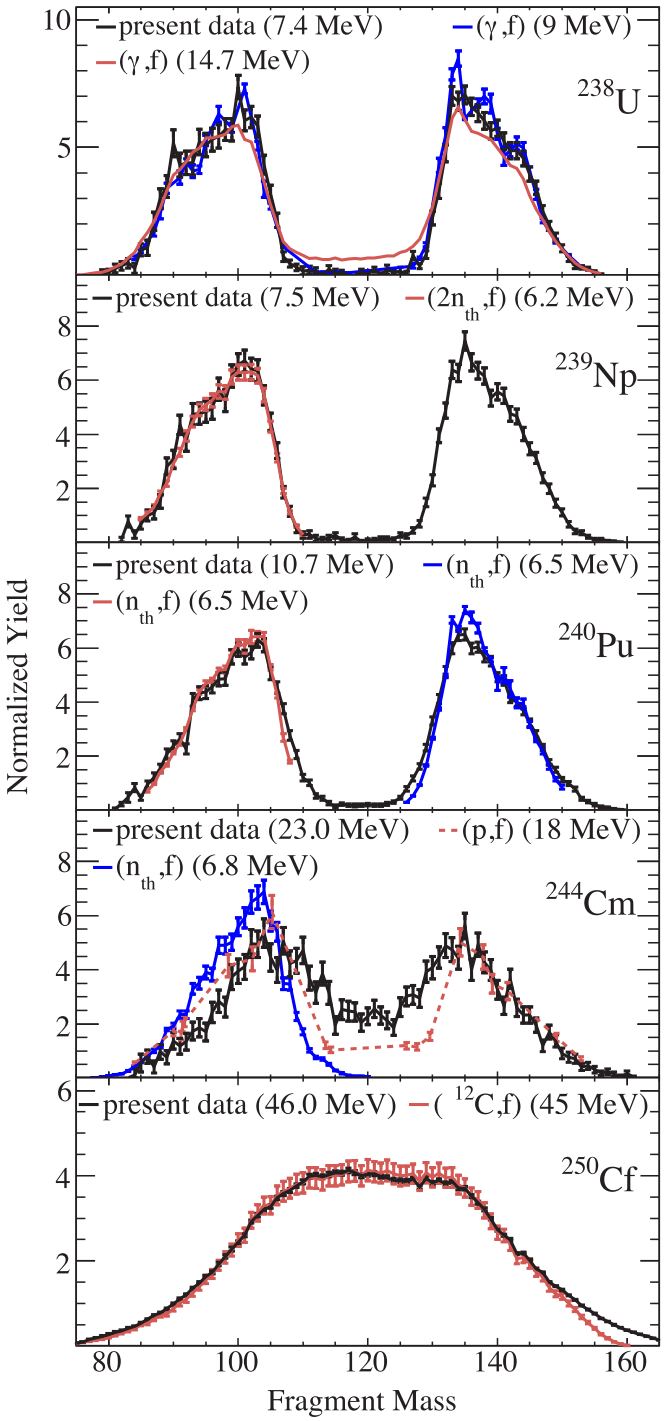

FIG. 19. Fission-fragment mass yields. Present data are compared with previous data in different energy ranges [6,9,13,29,30,35,47,48]. The corresponding E_x are indicated in parentheses.

excitation increases the probability of neutron evaporation. This variation is stronger in the region of heavy fragments than for light fragments, where the variation is almost negligible [32]. Thus, the yields from Coulomb-induced fission in the heavy region are shifted to lighter masses with respect to the present data while the yields in the light region are almost unaffected. A better agreement is observed with the data from Bremsstrahlung-induced fission, with more similar E_x, although large fluctuations are observed in these data around $A \in [135,145]$, not present in the other sets. These fluctuations might result from the measurement technique, which relies on knowledge of the level scheme of the populated fragments.

Concerning ^{239}Np, an excellent agreement is observed between present data and data from $2n_{\text{th}}$-induced fission [35], which has similar E_x. Larger angular momentum is expected to be transferred to the system for transfer reactions compared with neutron capture; however, from this comparison, no major effect is observed in the fragment mass distribution.

In ^{240}Pu, the agreement between present data and thermal neutron-induced fission from [29] and [6] is also good, taking into account the difference in E_x. The lower E_x of neutron-induced fission produces a deeper valley at symmetry, with more pronounced slopes at $A \approx 105$ and $A \approx 130$. The structure observed at $A \approx 101$, where the yield is lower than for the neighbors, is also reported in [29]. In the heavy region, neutron-induced fission, at lower E_x, results in a higher maximum at $A \approx 106$ and a narrower distribution, consistent with the observed features in the case of ^{238}U.

The mass distribution of ^{244}Cm is compared with thermal-neutron-induced fission from Ref. [30], where only the light fragment was measured, and with 12 MeV proton-induced fission from Ref. [48], where only the yields of fragments with well-known level schemes are identified. The evolution of the system as a function of E_x is evident: the system presents a strong asymmetric and no symmetric component for the lowest excitation energies. As expected, symmetric fission increases with increasing E_x. The large difference in E_x permits to observe this effect not only in the heavy fragment but also in the light fragment.

^{250}Cf is compared with a previous measurement [9] performed with a similar setup. The distributions are virtually identical up to $A > 150$, where, as discussed in Sec. IV A, the difference originates from experimental limitations in the previous measurement.

The above comparisons with previous data exhibit the strength of the experimental method used in this work and provide a clear observation of the effect of E_x on the fragment production: higher E_x feeds symmetric fission and affects the yields in the heavier group while the light group is less sensitive to limited E_x variations.

Figure 20 presents the ratio between the peak and the valley of the mass yield distribution as a function of E_x. This parameter represents the competition between symmetric and asymmetric fission, which is strongly dependent on E_x. Present data of ^{238}U and ^{240}Pu are compared with previous measurements. For U, present data are compared with neutron-induced fission of ^{239}U [49]. As shown in Fig. 17, symmetric fission increases for lighter isotopes; therefore, a lower peak-to-valley ratio would be expected for ^{238}U. The comparison reveals a good agreement despite the isotopic difference. Concerning Pu, the present measurement is in a rather good agreement with the trend described by the data from Ref. [50] (in blue). However, an additional measurement in the thermal neutron region [51] (in green) shifts the value slightly higher, which is

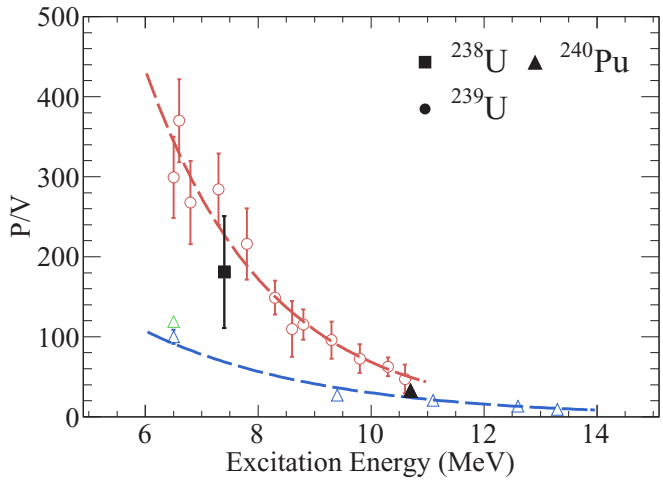

FIG. 20. The peak-to-valley ratio as a function of the excitation energy. Present data (in black) are compared with previous measurements of ^{239}U from [49] (in red) and of ^{240}Pu from [50] (in blue) and [51] (in green).

in better agreement with present data. In general, the agreement with previous measurement proves the good assignment of E_x in the present work.

Populating similar fissioning isotopes in a neutron-induced reaction implies neutron energies for which experimental information on isotopic yields is at present scarce, if not null. For example, the reactions ^{237}U(n,f), ^{238}Np(n,f), and ^{239}Pu(n,f), would require fast neutrons with $E_n = 1.26$, 1.28, and 4.19 MeV, respectively. Such data are of importance from an application point of view at present and future nuclear reactors. In particular, fission yields of ^{243}Pu(n,f) have a direct application in the heating calculations of current reactors. As a consequence, the present data, populating the same systems in surrogate transfer-induced reactions, can be used to supplement the missing neutron data.

V. CONCLUSIONS

The present work provides new experimental data on the full isotopic, elemental, and mass distributions of fission fragments on ^{238}U, ^{239}Np, ^{240}Pu, ^{244}Cm, and ^{250}Cf, at various initial excitation energy. These new data have been obtained by means of a innovative experimental technique, benefiting (i) from the possibility provided by transfer reactions to study several systems in a single experiment, while measuring their excitation energy, and (ii) from the combined use of inverse kinematics and the powerful VAMOS spectrometer at GANIL for complete coverage of the fission production, and accurate determination of the corresponding isotopic yields, respectively.

Good agreement with previous measurements is observed whenever available. As compared to previous information, the entire fragment production is covered, and unprecedented resolution in mass and charge is achieved. The larger angular momentum populated in these reactions was observed to contribute to second order on the fragment distributions, making the present data comparable with fast neutron-induced fission. The peak-to-valley ratio validates the surrogate method and confirms that the excitation energy populated in the transfer reactions corresponds, indeed, to the excitation energy of the fissioning system.

Together with the population of several fissioning systems in a single experiment, the quality of the data demonstrates the strength of the experimental approach. The variety of the available observables, and the corresponding physics output, are the subject of a forthcoming publication.

ACKNOWLEDGMENTS

This work was partially supported by the Spanish Ministry of Research and Innovation under the budget items FPA2010-22174-C02-01 and RYC-2012-11585. D.R. thanks A. Lemasson (GANIL) for his help and fruitful discussions during the data analysis. Also, the excellent support from the GANIL staff during the experiment is acknowledged.

[1] K.-H. Schmidt *et al.*, Nucl. Phys. A **665**, 221 (2000).
[2] W. Lang *et al.*, Nucl. Phys. A **345**, 34 (1980).
[3] U. Quade *et al.*, Nucl. Phys. A **487**, 1 (1988).
[4] J. P. Bocquet *et al.*, Z. Phys. A **335**, 41 (1990).
[5] E. Cheifetz *et al.*, Phys. Rev. C **4**, 1913 (1971).
[6] A. Bail, O. Serot, L. Mathieu, O. Litaize, T. Materna, U. Köster, H. Faust, A. Letourneau, and S. Panebianco, Phys. Rev. C **84**, 034605 (2011).
[7] I. Nishinaka, Y. Nagame, K. Tsukada, H. Ikezoe, K. Sueki, H. Nakahara, M. Tanikawa, and T. Ohtsuki, Phys. Rev. C **56**, 891 (1997).
[8] A. Bogachev *et al.*, Eur. Phys. J. A **34**, 23 (2007).
[9] M. Caamaño, O. Delaune, F. Farget, X. Derkx, K.-H. Schmidt, L. Audouin, C.-O. Bacri, G. Barreau, J. Benlliure, E. Casarejos, A. Chbihi, B. Fernández-Domínguez, L. Gaudefroy, C. Golabek, B. Jurado, A. Lemasson, A. Navin, M. Rejmund, T. Roger, A. Shrivastava, and C. Schmitt, Phys. Rev. C **88**, 024605 (2013).
[10] C. Rodríguez-Tajes *et al.*, Phys. Rev. C **89**, 024614 (2014).
[11] M. Caamaño and F. Farget, Phys. Lett. B **770**, 72 (2017).
[12] J. L. Rodríguez-Sánchez *et al.*, Phys. Rev. C **91**, 064616 (2015).
[13] E. Pellereau, J. Taïeb, A. Chatillon, H. Alvarez-Pol, L. Audouin, Y. Ayyad, G. Bélier, J. Benlliure, G. Boutoux, M. Caamaño, E. Casarejos, D. Cortina-Gil, A. Ebran, F. Farget, B. Fernández-Domínguez, T. Gorbinet, L. Grente, A. Heinz, H. Johansson, B. Jurado, A. Kelić-Heil, N. Kurz, B. Laurent, J.-F. Martin, C. Nociforo, C. Paradela, S. Pietri, J. L. Rodríguez-Sánchez, K.-H. Schmidt, H. Simon, L. Tassan-Got, J. Vargas, B. Voss, and H. Weick, Phys. Rev. C **95**, 054603 (2017).
[14] *International Evaluation Co-operation, Vol. 26*, NEA/WPEC-26 (OECD, Paris, 2008).
[15] A. Navin *et al.*, Phys. Lett. B **728**, 136 (2014).
[16] Y. H. Kim *et al.*, Phys. Lett. B **772**, 403 (2017).
[17] N. Fukuda *et al.*, Nucl. Instrum. Methods Phys. Res., Sect. B **317**, 323 (2013).

[18] F. Flavigny *et al.*, Phys. Rev. Lett. **118**, 242501 (2017).
[19] D. C. Biswas, R. K. Choudhury, B. K. Nayak, D. M. Nadkarni, and V. S. Ramamurthy, Phys. Rev. C **56**, 1926 (1997).
[20] S. Pullanhiotan *et al.*, Nucl. Instrum. Methods Phys. Res., Sect. A **593**, 343 (2008).
[21] M. Rejmund *et al.*, Nucl. Instrum. Methods Phys. Res., Sect. A **646**, 184 (2011).
[22] J. Simpson *et al.*, Acta Physica Hungarica, New Ser. **11**, 159 (2000).
[23] A. Shrivastava, M. Caamaño, M. Rejmund, A. Navin, F. Rejmund, K.-H. Schmidt, A. Lemasson, C. Schmitt, L. Gaudefroy, K. Sieja, L. Audouin, C. O. Bacri, G. Barreau, J. Benlliure, E. Casarejos, X. Derkx, B. Fernández-Domínguez, C. Golabek, B. Jurado, T. Roger, and J. Taieb, Phys. Rev. C **80**, 051305(R) (2009).
[24] S. Pullanhiotan *et al.*, Nucl. Instrum. Methods Phys. Res., Sect. B **266**, 4148 (2008).
[25] D. Ramos, Ph.D. thesis, University of Santiago de Compostela, 2016 (unpublished), http://hdl.handle.net/10347/15070
[26] E. Baron *et al.*, Nucl. Instrum. Methods Phys. Res., Sect. A **328**, 177 (1993).
[27] J. P. Dufour *et al.*, Nucl. Instrum. Methods Phys. Res., Sect. A **248**, 267 (1986).
[28] D. Bazin *et al.*, Nucl. Instrum. Methods Phys. Res., Sect. A **482**, 307 (2002).
[29] C. Schmitt *et al.*, Nucl. Phys. A **430**, 21 (1984).
[30] I. Tsekhanovich, N. Varapai, V. Rubchenya, D. Rochman, G. S. Simpson, V. Sokolov, G. Fioni, and I. Al Mahamid, Phys. Rev. C **70**, 044610 (2004).
[31] L. E. Glendenin, J. E. Gindler, D. J. Henderson, and J. W. Meadows, Phys. Rev. C **24**, 2600 (1981).
[32] K.-H. Schmidt and B. Jurado, Phys. Rev. Lett. **104**, 212501 (2010).
[33] R. Müller, A. A. Naqvi, F. Käppeler, and F. Dickmann, Phys. Rev. C **29**, 885 (1984).
[34] A. A. Naqvi, F. Käppeler, F. Dickmann, and R. Müller, Phys. Rev. C **34**, 218 (1986).
[35] G. Martínez *et al.*, Nucl. Phys. A **515**, 433 (1990).
[36] I. Tsekhanovich *et al.*, Nucl. Phys. A **688**, 633 (2001).
[37] K.-H. Schmidt *et al.*, Nucl. Data Sheets **131**, 107 (2016).
[38] V. M. Strutinsky, Nucl. Phys. A **95**, 420 (1967).
[39] J. Khuyagbaatar, D. J. Hinde, I. P. Carter, M. Dasgupta, C. E. Düllmann, M. Evers, D. H. Luong, R. du Rietz, A. Wakhle, E. Williams, and A. Yakushev, Phys. Rev. C **91**, 054608 (2015).
[40] K. Hirose, K. Nishio, S. Tanaka, R. Léguillon, H. Makii, I. Nishinaka, R. Orlandi, K. Tsukada, J. Smallcombe, M. J. Vermeulen, S. Chiba, Y. Aritomo, T. Ohtsuki, K. Nakano, S. Araki, Y. Watanabe, R. Tatsuzawa, N. Takaki, N. Tamura, S. Goto, I. Tsekhanovich, and A. N. Andreyev, Phys. Rev. Lett. **119**, 222501 (2017).
[41] J. N. Wilson, M. Lebois, L. Qi, P. Amador-Celdran, D. Bleuel, J. A. Briz, R. Carroll, W. Catford, H. De Witte, D. T. Doherty, R. Eloirdi, G. Georgiev, A. Gottardo, A. Goasduff, K. Hadynska-Klek, K. Hauschild, H. Hess, V. Ingeberg, T. Konstantinopoulos, J. Ljungvall, A. Lopez-Martens, G. Lorusso, R. Lozeva, R. Lutter, P. Marini, I. Matea, T. Materna, L. Mathieu, A. Oberstedt, S. Oberstedt, S. Panebianco, Z. Podolyak, A. Porta, P. H. Regan, P. Reiter, K. Rezynkina, S. J. Rose, E. Sahin, M. Seidlitz, O. Serot, R. Shearman, B. Siebeck, S. Siem, A. G. Smith, G. M. Tveten, D. Verney, N. Warr, F. Zeiser, and M. Zielinska, Phys. Rev. Lett. **118**, 222501 (2017).
[42] U. Brosa, S. Grossman, and A. Müller, Phys. Rep. **197**, 167 (1990).
[43] C. Böckstiegel *et al.*, Nucl. Phys. A **802**, 12 (2008).
[44] P. Möller and C. Schmitt, Eur. Phys. J. A **53**, 7 (2017).
[45] H. Paşca *et al.*, Nucl. Phys. A **969**, 226 (2018).
[46] M. Caamaño, F. Farget, O. Delaune, K.-H. Schmidt, C. Schmitt, L. Audouin, C.-O. Bacri, J. Benlliure, E. Casarejos, X. Derkx, B. Fernández-Domínguez, L. Gaudefroy, C. Golabek, B. Jurado, A. Lemasson, D. Ramos, C. Rodríguez-Tajes, T. Roger, and A. Shrivastava, Phys. Rev. C **92**, 034606 (2015).
[47] H. Naik *et al.*, Eur. Phys. J. A **49**, 94 (2013).
[48] T. Ohtsuki, Y. Hamajima, K. Sueki, H. Nakahara, Y. Nagame, N. Shinohara, H. Ikezoe, Phys. Rev. C **40**, 2144 (1989).
[49] F. Vivès, Nucl. Phys. A **662**, 63 (2000).
[50] H. Thierens, A. De Clercq, E. Jacobs, D. De Frenne, P. D'hondt, P. De Gelder, and A. J. Deruytter, Phys. Rev. C **23**, 2104 (1981).
[51] C. Wagemans, E. Allaert, A. Deruytter, R. Barthélémy, and P. Schillebeeckx, Phys. Rev. C **30**, 218 (1984).